Journal of Advanced Ceramics
2023, **12**(4): 734–746
https://doi.org/10.26599/JAC.2023.9220716
ISSN 2226-4108
CN 10-1154/TQ

Research Article

Broadband orange-emitting $Sr_3Si_8O_4N_{10}:Eu^{2+}$ phosphor discovered by a modified single-particle-diagnosis approach

Le Wang[a], Guozhen Ding[b], Shuxing Li[b], Shiro Funahashi[c], Takashi Takeda[c], Lu Yin[a], Pei Liang[a], Naoto Hirosaki[c], Rong-Jun Xie[b,d,*]

[a]*College of Optical and Electronic Technology, China Jiliang University, Hangzhou 310018, China*
[b]*Fujian Key Laboratory of Surface and Interface Engineering for High Performance Materials, College of Materials, Xiamen University, Xiamen 361005, China*
[c]*Phosphors Group, National Institute for Materials Science, Tsukuba 305-0035, Japan*
[d]*State Key Laboratory of Physical Chemistry of Solid Surfaces, Xiamen University, Xiamen 361005, China*

Received: November 16, 2022; Revised: December 31, 2022; Accepted: January 3, 2023

Abstract: Discovery of new phosphors with desired properties is of great significance for developing high optical quality solid-state lighting. The single-particle-diagnosis approach is an effective way to search novel phosphors by analyzing tiny single crystals screened from the fired powder mixtures. In this work, a broadband orange-emitting phosphor of $Sr_3Si_8O_4N_{10}:Eu^{2+}$ for solid state lighting was discovered by this method. The new oxonitridosilicate crystallizes in the monoclinic space group of $P2_1/n$ (No. 14) with cell parameters of a = 4.8185 Å, b = 24.2303 Å, c = 10.5611 Å, β = 90.616°, and Z = 4. The crystal structure of $Sr_3Si_8O_4N_{10}$ was determined from the single-crystal X-ray diffraction (XRD) data of a single crystal, which is made up of a three-dimensional framework consisting of vertex-sharing SiN_4 and SiN_3O tetrahedra. Sr^{2+} ions occupy five crystallographic sites and have coordination numbers between 6 and 8 with one ordered Sr and other four disordered Sr atoms. The multiple Sr sites lead to a broadband emission centered at 565–600 nm and a bandwidth of 128–138 nm. The internal and external quantum efficiencies (IQE/EQE) of the title phosphor are 48.6% and 29.1% under 450 nm excitation, respectively. To improve the accuracy and speed of distinguishing phosphor particles in fired powder mixtures, a microscopic imaging spectroscopy is developed and demonstrated to modify the single-particle-diagnosis method.

Keywords: oxonitridosilicate; phosphor; photoluminescence (PL); solid-state lighting; imaging spectroscopy

1 Introduction

Phosphor-converted white light-emitting diodes (pc-wLEDs) are generally considered as the most economical energy-saving and reliable lighting sources [1]. Phosphor is a key material that determines the performance of pc-wLEDs, such as luminous efficacy, color rendering index, and correlated color temperature and lifetime. With continuous advances in solid-state lighting, novel phosphors with enhanced or desired properties are in great demands. During the

* Corresponding author.
E-mail: rjxie@xmu.edu.cn

past decades, (oxo)nitridosilicates have been witnessed as main materials for phosphors due to their excellent chemical stability and structural diversity [2]. Wherein, a variety of promising (oxo)nitridosilicate phosphors have been developed and even commercialized, such as $M_2Si_5N_8$:Eu^{2+}, $MSiN_2$:Eu^{2+}/Ce^{3+}, $MSi_2O_2N_2$:Eu^{2+} (M = Ca, Sr, and Ba), $Ba_3Si_6O_{12}N_2$:Eu^{2+}, $Sr_3Si_2O_4N_2$:Eu^{2+}/ Ce^{3+}, $CaAlSiN_3$:Eu^{2+}/Ce^{3+}, Ca/Li-α-SiAlON:Eu^{2+}/Ce^{3+}, and β-SiAlON:Eu^{2+}/Ce^{3+} [3–13]. The Sr–Si–O–N chemical space has attracted great attention because the elements are earth-abundant, and Sr^{2+} can be substituted by luminescence centers of Eu^{2+} or Ce^{3+}. However, till now, only $SrSi_2O_2N_2$:Eu^{2+} and $Sr_3Si_2O_4N_2$:Eu^{2+} have been reported as phosphors in the Sr–Si–O–N system. It is believed that there is much room left to mine novel compounds enabling interesting luminescence.

Several interesting strategies superior to the traditional "trial-and-error" have been proposed to develop novel phosphors, such as the combinatorial chemistry method, mineral-inspired chemical unit substitution, high-throughput calculation prediction, and machine learning [14–17]. Park *et al*. [18–21] discovered several nitride phosphors (i.e., $Ba(Si,Al)_5(O,N)_8$:Eu^{2+}, $Ca_{1.5}Ba_{0.5}Si_5O_3N_6$:$Eu^{2+}$, $Ca_{15}Si_{20}O_{10}N_{30}$:$Eu^{2+}$, and $Ce_{4-x}Ca_xSi_{12}O_{3+x}N_{18-x}$:$Eu^{2+}$) by using a heuristic optimization-assisted combinatorial chemistry method, which requires an iterative powder processing procedure. Zhao *et al*. [22–25] proposed a mineral-inspired method and discovered several interesting phosphors, such as $RbLi[Li_3SiO_4]_2$:Eu^{2+}, $RbNa[Li_3SiO_4]_2$:Eu^{2+}, $RbNa_3[Li_3SiO_4]_4$:Eu^{2+}, and $CsNa_2K[Li_3SiO_4]_4$:Eu^{2+}. The key of this method is to find an original mineral-structure model. By growing large-size single crystals, Pust *et al*. [26–28] and Wagatha *et al*. [29] discovered a variety of red-emitting phosphors with narrow band emissions, including $M[LiAl_3N_4]$:Eu^{2+} (M = Ca and Sr) and $M[Mg_2Al_2N_4]$:Eu^{2+} (M = Ca and Sr). Ha *et al*. [30] reported a yellow-emitting phosphor of Sr_2LiAlO_4:Eu^{2+} in the Sr–Li–Al–O system by the data-driven structure prediction. Using the similar technique, Li *et al*. [31] found a super-broadband white-emitting phosphor of $Sr_2AlSi_2O_6N$:Eu^{2+}. Zhuo *et al*. [17] calculated the band gap (E_g) and Debye temperature (Θ_D) of 2071 compounds through machine learning, and successfully screened out a thermally robust blue phosphor of $NaBaB_9O_{15}$:Eu^{2+}. The data-driven method has become a powerful tool to accelerate the discovery of new phosphors, but it is based on the limited database of phosphors with simple or ordered crystal structures, and there are no effective ways to calculate or predict those with disordered structures.

By contrast, the single-particle-diagnosis approach, proposed by Hirosaki *et al*. [32], has great advantages in exploring novel phosphors with complicated chemical compositions or crystal structures as it is based on experiments rather than calculations. In this method, tiny single crystals (< 20 μm in size) are firstly distinguished from fired powder mixtures by a digital optical microscope, and then pinpointed for crystal determination in a single-crystal X-ray diffractometer and for photoluminescence (PL) property measurements in a single-particle fluorescence spectrometer. Several Eu^{2+}-doped nitride phosphors were discovered by this method, such as $Sr_3Si_{8-x}Al_xO_{7+x}N_{8-x}$:$Eu^{2+}$, $Sr_2B_{2-2x}Si_{2+3x}Al_{2-x}N_{8+x}$:$Eu^{2+}$, $Sr_{3.61}LiSi_{14.27}Al_{5.61}O_{6.19}N_{23.25}$:$Eu^{2+}$, $La_{2.85}Sr_{0.76}LiSi_{14.86}Al_{4.93}O_{2.89}N_{26.51}$:$Eu^{2+}$, and $La_{26-x}Sr_xSi_{41}O_{x+1}N_{80-x}$:$Eu^{2+}$ [33–36]. However, in this method, luminescent particles are only simply detected and selected by the naked eyes, and some of them with similar emitting colors will be missed no matter how differences in their spectral position and band width or even activators. To improve the precision and efficiency of identifying different emitting particles, a microscopic imaging spectroscopy needs to be built for precisely distinguishing those phosphor particles that cannot be recognized by human eyes.

In this contribution, we navigate the chemical space of Sr–Si–O–N (Sr_3N_2–Si_3N_4–SiO_2) and discover a novel orange-emitting phosphor $Sr_3Si_8O_4N_{10}$:Eu^{2+} by using the single-particle-diagnosis approach. The crystal structure and PL properties of the phosphor are investigated and discussed. We also develop a microscopic imaging spectroscopy and demonstrate to classify and distinguish phosphor particles with different emission spectra.

2 Experimental

2.1 Synthesis of phosphor powders

To explore new phosphors in the Sr–Si–O–N system, a variety of powder mixtures were prepared by mixing appropriate amounts of Sr_3N_2 (99.9%, Alfa Aesar, China), Si_3N_4 (99.99%, UBE Industries Ltd., Japan), SiO_2 (99.9%, Xilong Scientific, China), and Eu_2O_3 (99.9%, Alfa Aesar, China). In a composition triangle of Sr_3N_2–Si_3N_4–$3SiO_2$, twenty samples with Sr_3N_2 : Si_3N_4 : $3SiO_2$ = (0–0.5) : (0.5–1) : (0–0.1) were prepared.

2 g of each powder mixture was filled into a boron nitride (BN) crucible, and then fired in a gas-pressure sintering furnace (FVPHR-R-10, FRET-40, Fuji Dempa Kogyo, Japan) at 1800 ℃ for 2 h under 1.0 MPa N_2 pressure. The fired powder samples were then used to screen small single crystals. For the scale-up synthesis, powder mixtures with the nominal compositions of $Sr_{3-3x}Si_8O_4N_{10}:3xEu^{2+}$ (x = 1–5 at%) represents the Eu concentration) were fired at 1720 ℃ for 4 h under 1.0 MPa N_2 pressure (VESTA, Shimadzu, Japan).

2. 2 Characterizations

The phase purity was characterized by an X-ray diffractometer (D8 Advance, Bruker, Germany) with Cu Kα radiation (λ = 0.15406 nm) at 40 kV and 40 mA. The data were collected in the range of 2θ = 10°–90° by a step-scan mode with a step size of 0.0163° and a count time of 0.1 s/step. The illumination images and morphologies of the samples were taken by an optical microscope equipped with a fluorescence system (DP74, Olympus, Japan). The chemical composition was measured by using an inductively coupled plasma-mass spectrometer (ICP-MS; iCAP 7000 Plus, Thermo Fisher Scientific, Japan). The nitrogen and oxygen contents were measured via the selective hot-gas extraction instrument (TC-436, LECO, Japan). The microstructures of the fired powder samples were observed by a field-emission scanning electron microscope (FE-SEM; SU70, Hitachi, Japan) operated at 20 kV. The elemental compositions and distributions of the powder samples were acquired by an energy-dispersive X-ray spectrometer (X-MaxN, Oxford Instruments, UK).

The diffuse reflectance spectra were measured by an ultraviolet–visible (UV–Vis) spectrophotometer (UV-3600 Plus, Shimadzu, Japan) at room temperature. The PL spectra were measured by a steady-state fluorescence spectrometer (FLS980, Edinburgh Instruments, UK) equipped with a 450 W Xe lamp. The decay curves were recorded by using the μF920H-pulsed Xe flashlamp as the excitation source with a pulse repetition rate of 100 Hz. The quantum efficiency (QE) was measured with an absolute PL quantum yield spectrometer (Quantaurus-QY, Hamamatsu Photonics, Japan). The temperature-dependent PL was tested by a home-built system, which consists of a 365 nm LED light source, a temperature-controlled stage (THMS600E, Linkam, UK), and a charge-coupled device (CCD) spectrometer (USB2000+, Ocean Optics, USA), in a temperature range from 298 K (24.85 ℃) to 573 K (299.85 ℃) with a step of 25 K and a heating rate of 50 K/min. The thermal degradation of the phosphor was evaluated by a moisture-assisted method described in Ref. [37], where the sample was aged at a temperature of 200 ℃ and a humidity of 100% for varying periods.

The ^{29}Si solid-state nuclear magnetic resonance (SS-NMR) spectra were collected by using a 400 MHz SS-NMR spectrometer (Advance III, Bruker, Germany). The X-ray photoelectron spectroscopy (XPS) measurement was done with an X-ray photoelectron spectrometer (PHI Quantum 2000, Ulvac-Phi, Inc., Japan).

2. 3 Computation methods

The first principles method based on the plane wave pseudopotential implemented in the Vienna *ab initio* simulation package (VASP) code was carried out to optimize the geometric structure of the crystal, find the minimum energy (stable) position, and then illustrate the most stable site of the substitution site for Eu^{2+} [38,39]. The crystal usually exhibits its actual properties in stable positions. The geometry optimization was carried out by using the generalized gradient approximation (GGA) functional. The Perdew–Burke–Ernzerhof (PBE) functional is a form of the GGA functional for exchange-correlation interactions. The total energy was obtained by the self-consistent solving of the Kohn–Sham equation.

In all calculations, the plane wave cut-off energy was 500 eV, all structural high symmetry points (k-points) were generated using VASPKIT software, the structure was optimized, the accuracy was 0.01 × 2π $Å^{-1}$ using the Gamma Scheme, and the optical properties were calculated with an accuracy of 0.01 × 2π $Å^{-1}$. All structures were fully relaxed using the Birch–Murnaghan equation of state until the force on each atom was less than 0.01 eV/Å. In the finite strain theory, stress is modeled by applying a uniform set of strains (a scaling factor of the lattice constant) to relax the freedom of the atoms, thereby calculating the resulting external stress. The anion positions are kept consistent and randomly selected on the main phase, and reasonable calculations show that changes in the anion atomic positions in the monomer do not change the final gap values and energy band structure when the anion atomic density ratio is constant. In our structure model for calculations, it contains 100 atoms,

e.g., 1 Eu, 11 Sr, 32 Si, 16 O, and 40 N atoms. Three different models of Eu substituting Sr_1, Sr_2, and Sr_3 were used for calculations, and then evaluated the minimum energy position as the most favorite substitution site for Eu^{2+}.

2. 4 Setup of microscopic imaging spectroscopy

The home-built microscopic imaging spectroscopy consists of a microscopy hyperspectral imaging spectrometer (Lumetta, Horiba Scientific, Japan) and UV-LED, as shown in Fig. 1. The excitation light from the UV-LED is reflected by a long wavelength pass filter towards objective lens, and then collimated by an objective lens. The mixed powders are illuminated and usually emit multi-colors. The emitting light containing superimposed spectra is collected by an objective lens and goes through the long wavelength pass filter. The light is then focused at the entrance slit of the imaging spectroscopy, and then collimated and dispersed, and finally is again focused on the detector. The data obtained by the array detector are the intensity and spectral distribution of a linear field of view, and then linear scanning is necessary by using an electric moving stage to obtain three-dimensional (3D) imaging spectral data. The processing flow of data is given in Fig. 2.

3 Results and discussion

3. 1 Discovery of new orange-emitting phosphor

As shown in Fig. 3(a), an orange-emitting single particle is observed from the powder mixture upon excitation by a UV-LED, and then pinpointed from a crucible for the single-crystal X-ray diffraction (XRD) analysis. The red-emitting particles in the powder mixture are identified as $Sr_2Si_5N_8:Eu^{2+}$ by the powder XRD. The single-crystal XRD results confirm that the orange phosphor particle is a new compound that has never been reported. The compound belongs to a monoclinic space group of $P2_1/n$ (No. 14) with cell parameters of a = 4.8185 Å, b = 24.2303 Å, c = 10.5611 Å, and β = 90.616° (Table 1). The chemical

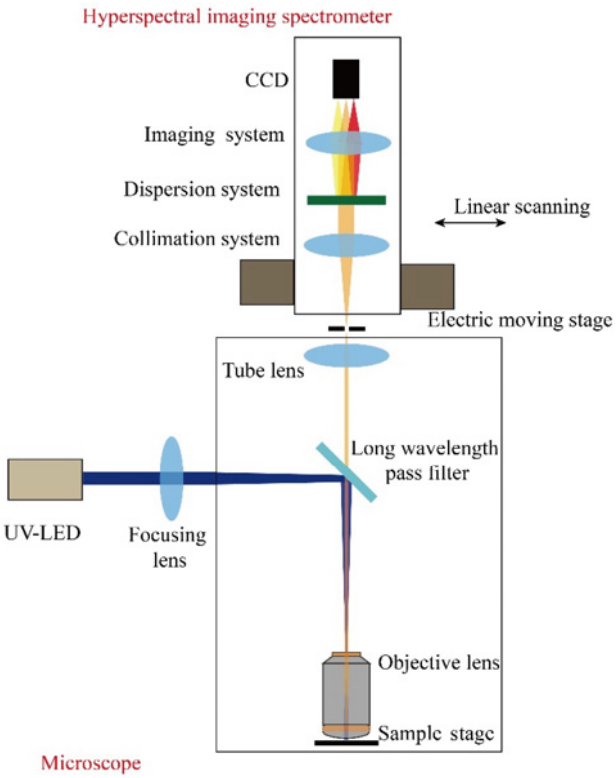

Fig. 1 Schematic of microscopic imaging spectroscopy.

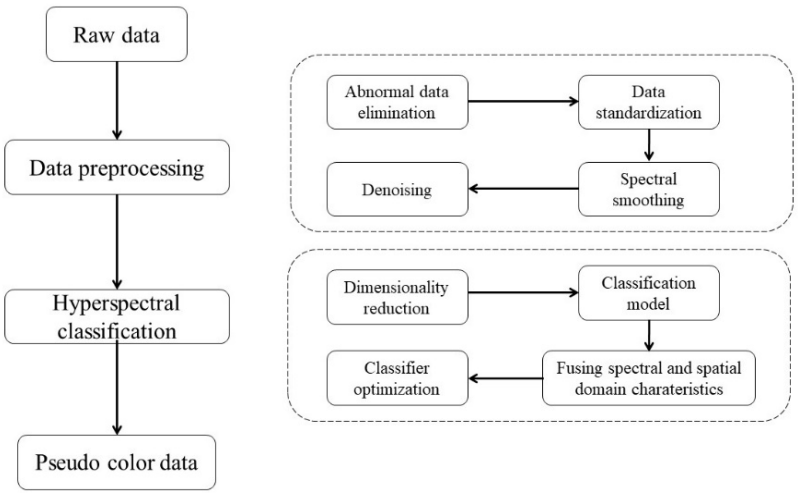

Fig. 2 Chart of hyperspectral data processing flow.

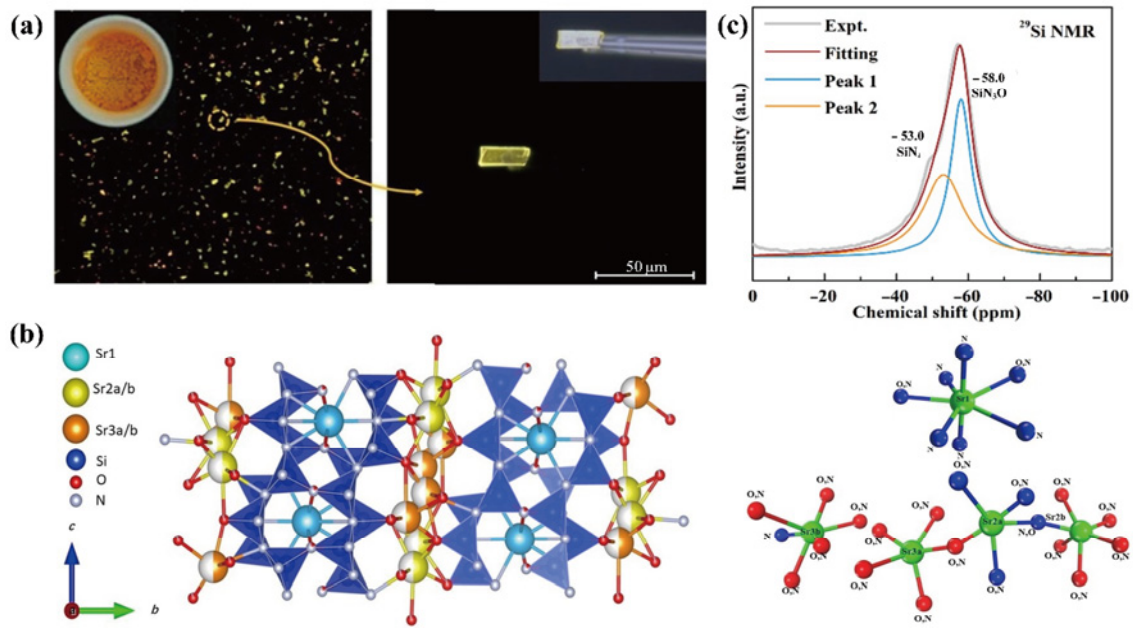

Fig. 3 (a) Single crystal pinpointed from fired powder mixture; (b) crystal structures of $Sr_3Si_8O_4N_{10}$ projected along [100] and five different coordination environments for Sr; and (c) solid-state ^{29}Si NMR spectra of $Sr_3Si_8O_4N_{10}$.

Table 1 Crystallographic data and structure refinement of $Sr_3Si_8O_4N_{10}$

Formula	$Sr_3Si_8O_4N_{10}$
Molecular weight (g/mol)	691.60
Crystal system	Monoclinic
Space group	$P2_1/n$
Temperature (K)	301
Information about the diffractometer	Oxford diffraction (ROD), Synergy custom system, HyPix-Arc 150
Radiation source	Microfocus rotating-anode X-ray generator “FR-X”, Rigaku, (Mo) X-ray source
Radiation	Mo Kα
λ (Å)	0.71073
a (Å)	4.8185(1)
b (Å)	24.2303(3)
c (Å)	10.5611(1)
V (Å^3)	1232.98(3)
β (°)	90.616(1)
Z	4
$\rho_{calculated}$ (g/cm^3)	3.726
F(000)	1297.860
μ (mm^{-1})	13.76
Crystal size (mm × mm × mm)	0.03 × 0.01 × 0.003
Diffraction range	$3.34° \leqslant \theta \leqslant 30.00°$
Index range	$-8 \leqslant h \leqslant 5, -40 \leqslant k \leqslant 40$, and $-17 \leqslant l \leqslant 17$
Total number of reflection	91,370
Independent reflection	5958
Observed reflection	5115 ($R_{int} = 0.054$)
Refined parameter	369
Absorption correction	Multi-scan
Refinement on F2	$R(F^2 > 2\sigma(F^2)) = 0.030$, $wR(F^2) = 0.072$, $S = 1.09$
	$w = 1/[\sigma^2 F_{o^2} + (0.0263P)^2 + 4.1391P]$, where $P = (F_{o^2} + 2F_{c^2})/3$
	$(\Delta/\sigma)_{max} = -0.001$; $\Delta\rho_{max} = 1.73$ e·Å^{-3}; $\Delta\rho_{min} = -1.56$ e·Å^{-3}

compositions of the single crystal were analyzed as Sr : Si : O : N : Eu = 2.97 : 7.00 : 3.97 : 8.69 : 0.02, which is thus determined to be $Sr_3Si_8O_4N_{10}$ as the main compound.

$Sr_3Si_8O_4N_{10}$ contains a highly condensed network structure built up on vertex-sharing SiN_4 and SiN_3O tetrahedra (Fig. 3(b)). This leads to a condensation degree (k) of 0.571. The ^{29}Si NMR spectra show two signal peaks at −53.0 and −58.0 ppm, assigned to two different local coordination environments for Si, i.e., SiN_4 and SiN_3O, respectively (Fig. 3(c)). The peaks were fitted into two Lorentzians with an integrated intensity ratio of 1 : 1, which is consistent with its crystal structure. All Si–(N,O) bond lengths (1.5894–1.7792 Å) are in the typical range of (oxo)nitridosilicates. Tetrahedral angles of N–Si–(N,O) range from 103.80° to 115.94° for edge-sharing $Si(N,O)_4$ tetrahedra. The tetrahedra form two types of channels along the [100] direction, i.e., cage- and layer-like ones, as shown in Fig. 3(b). There are five independent Wyckoff sites for Sr atoms in the unit cell of $Sr_3Si_8O_4N_{10}$. Among them, Sr1 atoms are located in the cage-like channel, coordinated to 6 N and 2 (N,O) atoms. The distances of Sr1–N and Sr1–(N,O) are between 2.6169 and 3.0923 Å with an average bond length of 2.8604 Å. The other four Sr atoms in the layer-like channel, Sr_{2a}, Sr_{2b}, Sr_{3a}, and Sr_{3b}, are mainly coordinated with (N,O) atoms. Sr_{2a} and Sr_{2b} equally share the same crystallographic site (i.e., the occupation fraction is 50% for each Sr atom), and it is also true for Sr_{3a} and Sr_{3b}. The Sr_{2a} is coordinated to 5 (N,O) atoms with distances lying in the range of 2.3710–2.7570 Å (average distance of 2.5226 Å), and the Sr_{2b} is connected to 1 N and 5 (N,O) atoms at distances of 2.3700–3.0230 Å (average distance of 2.6381 Å). The Sr_{3a} is linked by 1 N and 5 (N,O) atoms, and their distances are between 2.4160 and 3.0990 Å (average distance of 2.6881 Å); the Sr_{3b} is also coordinated to 1 N and 5 (N,O) atoms at distances of 2.3260–3.0660 Å (average distance of 2.6417 Å). The detailed structural parameters are summarized in Table 2.

3. 2 PL properties

The powder phosphors of $Sr_3Si_8O_4N_{10}:Eu^{2+}$ with varying Eu^{2+} concentrations in the range of 1–5 at% were also prepared by gas-pressure sintering, and the phase pure powders were finally obtained for PL property measurements. As shown in Fig. 4, these powders show a plate-like morphology, indicating the preferred growth of the particle. They emit yellow or orange colors depending on the x, observed by an optical microscope under 365 nm excitation. The elemental mappings demonstrate that Sr, Si, O, and N elements are homogeneously distributed within the phosphor particles. The average atomic ratio of Sr : Si : O : N : Eu = 2.97 : 8.8 : 5.7 : 8.1 : 0.03 acquired in the selected area by the energy dispersive spectroscopy (EDS) is in well accordance with the nominal composition of $Sr_{2.97}Si_8O_4N_{10}:0.03Eu^{2+}$.

The single phosphor particle of $Sr_{2.98}Si_8O_4N_{10}:0.02Eu^{2+}$ pinpointed from the powder mixture shows a broadband emission spectrum extending from 450 to 800 nm with a maximum at 571 nm and full width at half maximum (FWHM) of 120 nm under 365 nm excitation, measured by a home-built single-particle fluorescence spectrometer (Fig. 5(a)). For the scale-up synthesized phosphor powder samples, their emission spectra are quite similar to that of the single crystal. The emission is substantially red-shifted from 565 to 600 nm, and the FWHM increases from 128 to 138 nm when the x is increased from 1 to 5 at% (Figs. 5(b) and 5(c), respectively). Correspondingly, the chromaticity coordinates are gradually moved from the orange region (0.4532, 0.5089) to the orange–red region (0.5184, 0.4658) (Fig. 5(d)). The emission of the powder samples is usually longer than that of the single crystal of $Sr_3Si_8O_4N_{10}:Eu^{2+}$ owing to the reabsorption of phosphor powders [32]. In addition, the use of different fluorescence spectrometers for single crystals and powders may also cause the difference in the emission spectra.

A large FWHM is quite rare for Eu^{2+}. It is usually smaller than 100 nm, and depends on the local coordination environment of Eu^{2+} as well as the number of crystallographic sites where Eu^{2+} occupies. The emission spectrum becomes narrow when Eu^{2+} is located at a highly symmetric site, such as β-SiAlON:Eu^{2+} (FWHM = 55 nm), $Sr[LiAl_3]N_4:Eu^{2+}$ (FWHM = 50 nm), and $Sr[Be_6ON_4]:Eu^{2+}$ (FWHM = 35 nm) [3,27,40]. On the other hand, the FWHM becomes broader when there are multi-sites for Eu^{2+} in a host, such as $Sr_3Li_4Si_2N_6:Eu^{2+}$ (FWHM = 200 nm) and $Sr_2AlSi_2O_6N:Eu^{2+}$ (FWHM = 236 nm) [31,41]. The orange-emitting $Sr_3Si_8O_4N_{10}:Eu^{2+}$ has an FWHM larger than 120 nm, which is in good agreement with the result that there are five crystallographic sites of Sr^{2+}. It means that $Sr_3Si_8O_4N_{10}:Eu^{2+}$ enables to produce higher color rendition warm white light than

Table 2 Fractional atomic coordinates (*x*, *y*, *z*) and isotropic (U^*_{iso}) or equivalent (U_{eq}) isotropic displacement parameters

Atom	*x*	*y*	*z*	U^*_{iso} /U_{eq}	Occupancy
Sr01	0.41579(11)	0.22424(2)	0.29421(4)	0.00732(13)	1.0
Sr02	0.8672(2)	0.02555(5)	0.56298(11)	0.0150(3)	0.5
Sr03	0.6397(3)	0.01319(6)	0.68372(12)	0.0194(3)	0.5
Sr04	0.3813(3)	0.04249(5)	0.81532(16)	0.0270(4)	0.5
Sr05	0.8834(3)	0.00415(7)	0.06476(14)	0.0267(4)	0.5
Si01	0.91690(12)	0.14436(2)	0.79739(5)	0.00479(10)	1.0
Si02	0.41521(12)	0.32347(2)	0.57917(5)	0.00438(10)	1.0
Si03	0.40942(12)	0.40518(2)	0.79693(5)	0.00437(9)	1.0
Si04	0.41277(12)	0.11071(2)	0.45032(5)	0.00483(10)	1.0
Si05	0.41404(12)	0.10429(2)	0.14396(5)	0.00455(10)	1.0
Si06	0.41105(12)	0.31960(2)	1.01420(5)	0.00433(10)	1.0
Si07	0.41447(12)	0.19733(2)	0.65888(5)	0.00451(10)	1.0
Si08	0.41058(12)	0.19348(2)	0.93394(5)	0.00416(9)	1.0
O001	0.3713(4)	0.04335(7)	0.08856(19)	0.0146(3)	0.92211(352)
N001	0.3713(4)	0.04335(7)	0.08856(19)	0.0146(3)	0.07789(352)
O002	0.3614(4)	0.05428(8)	0.5232(2)	0.0173(4)	0.90918(352)
N002	0.3614(4)	0.05428(8)	0.5232(2)	0.0173(4)	0.09082(352)
O003	0.3516(4)	0.47020(7)	0.80213(17)	0.0128(3)	0.91361(352)
N003	0.3516(4)	0.47020(7)	0.80213(17)	0.0128(3)	0.08639(352)
O004	0.8912(4)	0.07834(7)	0.8026(2)	0.0174(4)	0.91801(352)
N004	0.8912(4)	0.07834(7)	0.8026(2)	0.0174(4)	0.08199(352)
O005	0.3429(4)	0.26015(7)	0.94510(17)	0.0090(3)	0.16523(352)
N005	0.3429(4)	0.26015(7)	0.94510(17)	0.0090(3)	0.83477(352)
O006	0.3715(4)	0.26563(7)	0.66050(17)	0.0086(3)	0.17186(352)
N006	0.3715(4)	0.26563(7)	0.66050(17)	0.0086(3)	0.82814(352)
N007	0.2657(4)	0.16672(7)	0.52514(16)	0.0060(3)	1.0
N008	0.7635(4)	0.39022(8)	0.79653(16)	0.0068(3)	1.0
N009	0.7633(4)	0.17647(8)	0.66548(16)	0.0062(3)	1.0
N010	0.7640(4)	0.17763(8)	0.92700(16)	0.0062(3)	1.0
N011	1.2607(4)	0.16814(7)	0.79381(16)	0.0059(3)	1.0
N012	0.2625(4)	0.37453(8)	0.92897(16)	0.0066(3)	1.0
N013	0.2622(4)	0.37887(8)	0.66019(16)	0.0064(3)	1.0
N014	0.2625(4)	0.15749(8)	0.05907(16)	0.0067(3)	1.0

Ca-α-SiAlON:Eu^{2+} (FWHM = 92 nm) [5,42]. In addition, the excitation spectrum of $Sr_3Si_8O_4N_{10}$:Eu^{2+} is much narrower than that of Ca-α-SiAlON:Eu^{2+}, which covers the range of 250–600 nm and has a maximum at 450 nm, indicating that the crystal field is not strong in $Sr_3Si_8O_4N_{10}$:Eu^{2+}. The crystal field strength is closely related to the coordination number and geometry of the substituted cation. Since Sr_1 has a larger coordination number and longer bond length than other four Sr atoms, we conclude that Eu^{2+} prefers to enter the Sr_1 site as it shows the smaller crystal field strength. To further confirm the preferred occupation of Eu, the total energies of different structure modes (with Eu occupying different Sr sites), calculated by the first principles method, were obtained. They are −726.173, −723.960, and −721.561 eV for Sr_1(Eu), Sr_2(Eu), and Sr_3(Eu), respectively. It therefore indicates that the Sr_1 site is the most favorable for Eu, and is in good agreement with the experimental data and the conclusion deduced from the coordination environment of Eu.

The diffuse reflectance spectra of $Sr_3Si_8O_4N_{10}$:Eu^{2+}

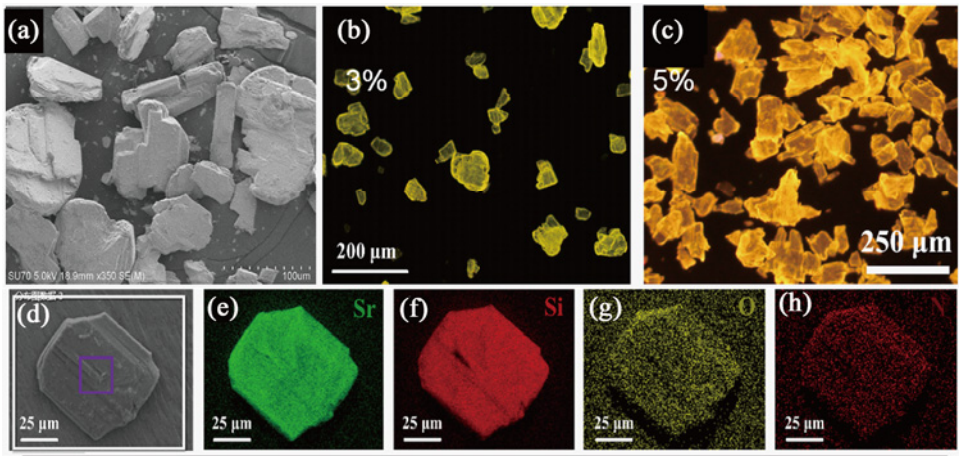

(i)	Sr	Si	O	N	Eu
(at%)	11.52	34.28	22.47	31.60	0.13
Average atom ratio	2.97	8.8	5.7	8.1	0.03

Fig. 4 Characterizations of $Sr_{3-3x}Si_8O_4N_{10}:3xEu^{2+}$ phosphor powders. (a) SEM image; (b, c) fluorescent microscopy photographs of $Sr_{3-3x}Si_8O_4N_{10}:3xEu^{2+}$ (x = 0.03 and 0.05) under 380 nm excitation; (d–h) EDS elemental mappings of Sr, Si, O, and N; and (i) contents of each element (at%) at the selected area in (d).

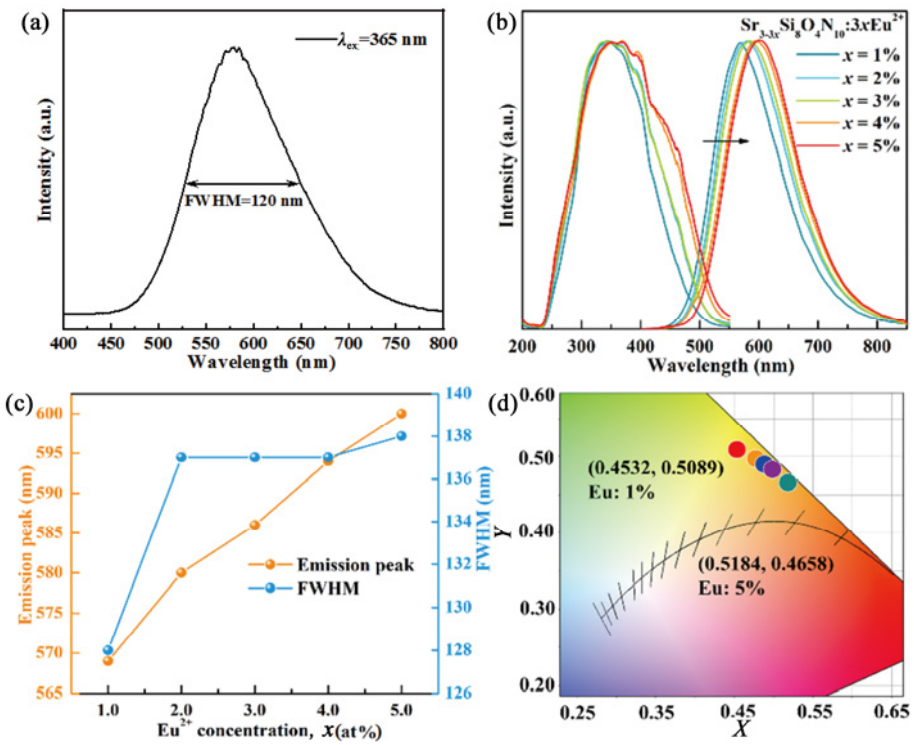

Fig. 5 PL spectra of $Sr_{3-3x}Si_8O_4N_{10}:3xEu^{2+}$. (a) Emission spectrum of single crystal pinpointed from the fired powder mixture; (b) emission and excitation spectra of $Sr_{3-3x}Si_8O_4N_{10}:3xEu^{2+}$ phosphor powders with varying x (1–5 at%); (c) maximum emission and FWHM as a function of x; and (d) chromaticity coordinates of phosphor powders with varying x.

with varying Eu contents display two primary absorption bands in the range of 250–550 nm (Fig. 6(a)). The weak band over 250–280 nm is originated from the host lattice, and the strong band spanning from 280 to 550 nm is attributed to the $4f^65d^1 \leftarrow 4f^7(^8S_{7/2})$ electronic transition of Eu^{2+}, the latter of which is intensified with the increasing Eu^{2+} concentration. As given in Fig. 6(b), under 450 nm excitation, the internal and external quantum efficiencies (IQE/EQE) have the maximal values of 48.6% and 29.1% under

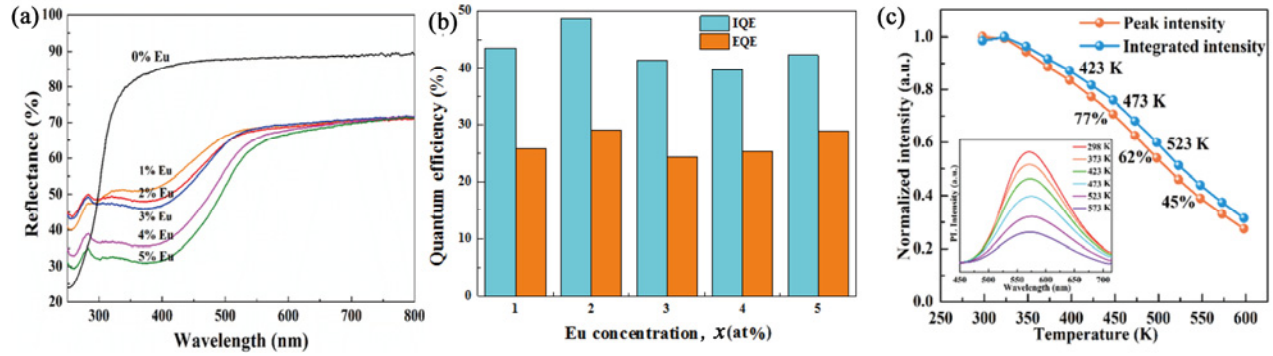

Fig. 6 (a) Diffuse reflectance spectra and (b) IQEs/EQEs of $Sr_{3-3x}Si_8O_4N_{10}:3xEu^{2+}$ phosphor powders under 450 nm excitation. (c) Temperature-dependent peak and integrated intensities of $Sr_{2.97}Si_8O_4N_{10}:0.03Eu^{2+}$ under 365 nm excitation. The inset in (c) is the emission spectra measured at different temperatures.

450 nm excitation for the sample with 2 at% Eu ($Sr_3Si_8O_4N_{10}:0.02Eu^{2+}$), respectively. In addition, the fluorescence lifetime of $Sr_3Si_8O_4N_{10}:Eu^{2+}$ was measured to be 0.83 and 1.24 μs when monitoring the emissions of 556 and 606 nm under 450 nm, respectively, which is in the range of several hundred nanoseconds to 2 μs for Eu^{2+}.

The temperature-dependent PL of $Sr_{2.97}Si_8O_4N_{10}:0.03Eu^{2+}$ is shown in Fig. 6(c). The PL declines with the increasing temperature due to the thermally induced lattice relaxation, and the sample can remain 77% of its PL intensity at 423 K (149.85 ℃). In general, the thermal quenching activation energy can be calculated according to Eq. (1) [43]:

$$I_T = \frac{I_0}{1 + A\exp\left(-\frac{\Delta E_q}{k_B T}\right)} \quad (1)$$

where I_T is the intensity at a given temperature (T), I_0 is the initial emission intensity, A is the pre-exponential factor, k_B is the Boltzmann's constant, and ΔE_q is the activation energy for thermal quenching. The ΔE_q is calculated to be 0.76 eV, comparable to that of $YAG:Ce^{3+}$ (0.77 eV) [44], indicating good thermal stability of $Sr_{2.97}Si_8O_4N_{10}:0.03Eu^{2+}$. In addition, ΔE_q can also be derived by Eq. (2):

$$\Delta E_q = T_{0.5}/680 \quad (2)$$

where $T_{0.5}$ is the thermal quenching temperature, at which the emission intensity decreases to 50% of its initial intensity. The $T_{0.5}$ is calculated to be 516 K (242.85 ℃), consistent with the experimental value of 510 K (236.85 ℃).

Furthermore, the thermal degradation of $Sr_{2.97}Si_8O_4N_{10}:0.03Eu^{2+}$ was evaluated by aging it under a saturated humidity (100%) condition at 200 ℃. The phase purity and the PL (spectral position and shape) almost remain unchanged after being treated for 256 h, implying strong thermal and chemical stability of the title phosphor (Fig. 7).

3.3 Valence state of Eu

To investigate the chemical valences of Eu, the XPS was conducted on $Sr_{2.97}Si_8O_4N_{10}:0.03Eu^{2+}$. All elements of Sr, Si, O, N, and Eu are detected on the full spectrum, as shown in Fig. 8(a). The fine spectrum of Eu indicates the coexistence of Eu^{2+} and Eu^{3+} (Fig. 8(b)). Specifically, in the Eu $3d_{3/2}$ region, the peak at the binding energy of 1154 eV belongs to Eu^{2+}; whereas in the Eu $3d_{5/2}$ region, the peak at the binding energy of 1124 eV belongs to Eu^{2+}, and the peak at 1133 eV is assigned to Eu^{3+}. Obviously, the signal of Eu^{2+} is much stronger than that of Eu^{3+}. The absolute amounts of Eu^{2+} and Eu^{3+} are calculated to be 0.43% and 0.11%, respectively. It thus indicates that Eu^{2+} ions are dominant in $Sr_{2.97}Si_8O_4N_{10}:0.03Eu^{2+}$ and contributes to the yellow or orange emission. No PL of Eu^{3+} (the sharp lines) is not detected in the sample due to the much higher energy levels of Eu^{3+}. The Eu^{3+} is not wanted in the Eu^{2+}-doped phosphors as it usually acts a luminescence killer [45].

3.4 Enhanced identification of luminescent particles by the microscopic imaging spectroscopy

In the single-particle-diagnosis approach, the phosphor particles are usually identified and picked up by their emission colors with a digital optical microscope under UV or blue light irradiation. In some cases, we cannot distinguish those phosphor particles with the same emission color but different emission spectra by the

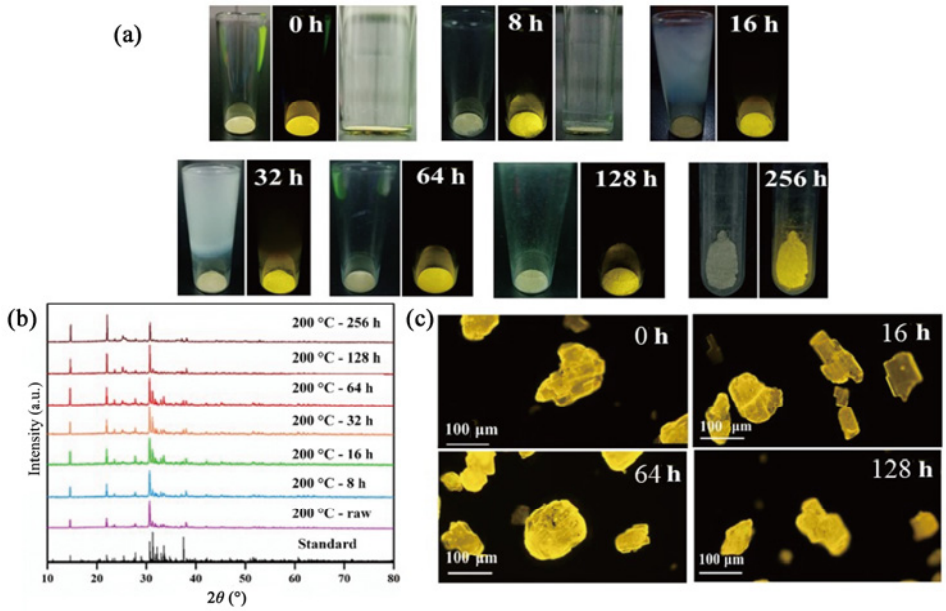

Fig. 7 (a) Photographs (left: under natural light; right: under UV light); (b) XRD patterns; and (c) fluorescent images of $Sr_{2.97}Si_8O_4N_{10}$:0.03Eu^{2+} sample aged at 200 ℃ and 100% humidity for varying time.

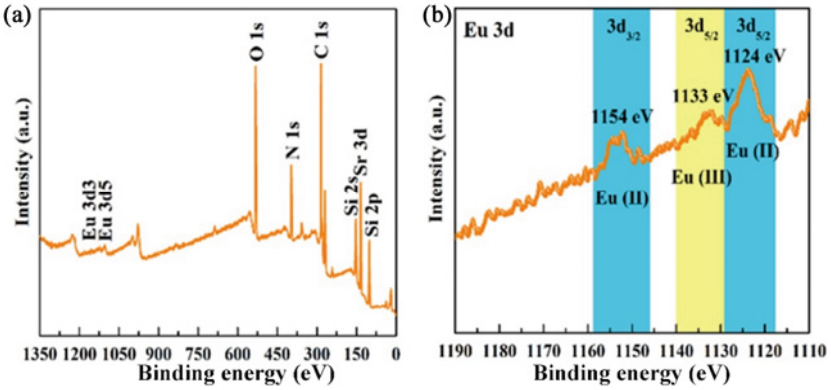

Fig. 8 XPS spectra of $Sr_{2.97}Si_8O_4N_{10}$:0.03Eu^{2+}. (a) Full spectrum and (b) fine spectrum of Eu.

naked eyes, which therefore may miss some phosphors with new crystal structures. The microscopic imaging spectroscopy, lying on the emission spectrum rather than emission color, would be a powerful tool to solve the problem.

As shown in Figs. 9(a) and 9(b), the phosphor particles, containing β-SiAlON:Eu^{2+} (λ_{em} = 550 nm and FWHM = 55 nm) and $Lu_3Al_5O_{12}$:Ce^{3+} (λ_{em} = 535 nm and FWHM = 125 nm), display almost the equal green emission color but different spectral shapes (positions and widths) under UV light excitation, making it hard to distinguish them with the naked eyes [3,46]. As we can see in Fig. 9(b), the noise of image is reduced compared to that in Fig. 9(a). As the original image is collected, the noise of the data is caused by the camera response, the illumination uniformity, or the spectrometer. The noise is random that is difficult to predict and eliminate accurately. The noise may affect the result of subsequent processing, so the preprocessing is to reduce the influence of noise. By using the microscopic imaging spectroscopy technique, each phosphor particle is quickly scanned, and the hyperspectral data containing space and spectral information of the mixed phosphor powders are collected. Then, the phosphor particles can be classified into two distinct colors (red for β-SiAlON:Eu^{2+} and green for $Lu_3Al_5O_{12}$:Ce^{3+}) by their emission spectra, as shown in Figs. 9(c)–9(e). This indicates that the imaging spectroscopy can replace human eyes to screen the phosphor particles with high accuracy and high speed, which would enhance the efficiency of the single-particle-diagnosis approach.

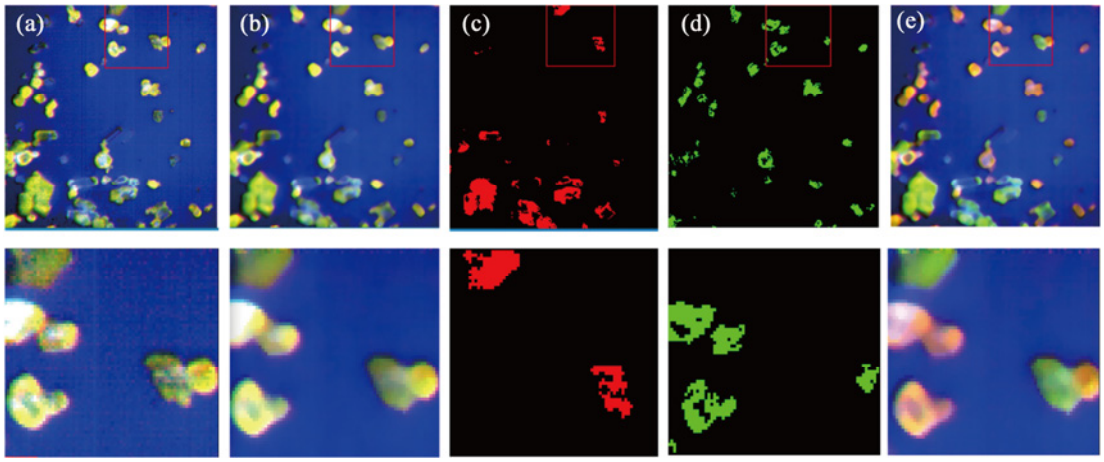

Fig. 9 (a) Raw data of mixed powders; (b) data after preprocessing; (c, d) results of classification; and (e) classified data in pseudo color.

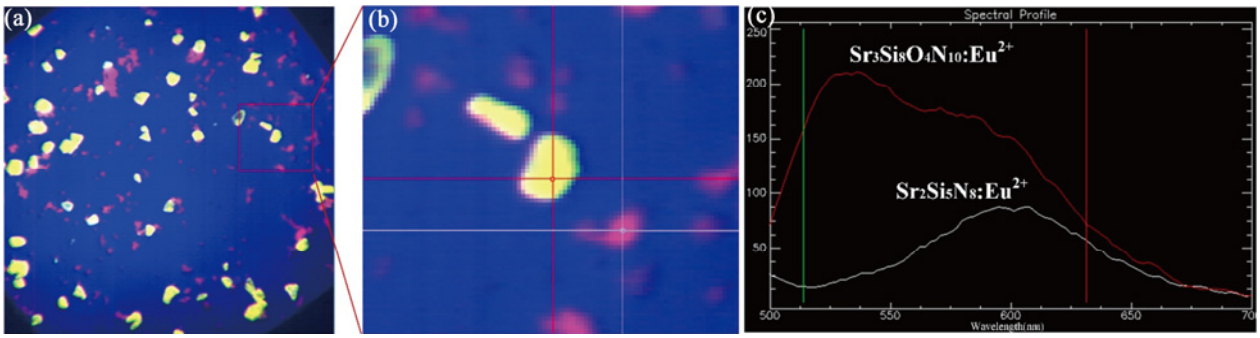

Fig. 10 Microscopic imaging spectroscopy images applied to the investigated powder mixture. (a, b) $Sr_3Si_8O_4N_{10}:Eu^{2+}$ (yellow) and $Sr_2Si_5N_8:Eu^{2+}$ (pink) particles in original field of view and the enlarged field of view, respectively; (c) emission spectra of $Sr_3Si_8O_4N_{10}:Eu^{2+}$ (red) and $Sr_2Si_5N_8:Eu^{2+}$ (white).

By applying the microscopic imaging spectroscopy in the investigated fired powder mixture, the emission spectra of two different $Sr_3Si_8O_4N_{10}:Eu^{2+}$ and $Sr_2Si_5N_8:Eu^{2+}$ phosphors are obtained, and then they are precisely identified and imaged with different colors (Fig. 10). The broadband emission of $Sr_3Si_8O_4N_{10}:Eu^{2+}$ is also observed by the imaging spectroscopy but with two distinct bands centered at ~540 and 580 nm. This will reduce the labor intensity, avoid the misjudgement by the naked eyes, and enhance the speed of screening of phosphor particles.

4 Conclusions

An orange-emitting $Sr_3Si_8O_4N_{10}:Eu^{2+}$ with a broadband emission was discovered in the Sr–Si–O–N system by the single-particle-diagnosis approach in this work. $Sr_3Si_8O_4N_{10}$ crystallizes in the monoclinic system ($P2_1/n$), and has lattice parameters of a = 4.8185 Å, b = 24.2303 Å, c = 10.5611 Å, β = 90.616°, and Z = 4, which is built up on the 3D networks of vertex-sharing SiN_4 and SiN_3O tetrahedra. $Sr_{3-3x}Si_8O_4N_{10}:3xEu^{2+}$ (x = 1–5 at%) shows a broadband emission centered at 565–600 nm and an FWHM of 128–138 nm. The orange emission is ascribed to the nitrogen-rich coordination and short bond length of Eu–(N,O), and the broadband is attributed to the multi-sites of Sr for Eu substitution. Under 450 nm excitation, the $Sr_3Si_8O_4N_{10}:0.02Eu^{2+}$ phosphor has an EQE of 29.1%. The microscopic imaging spectroscopy allows to precisely and quickly distinguish luminescent particles, which therefore adds values to the single-particle- diagnosis approach.

Acknowledgements

This work was supported by the National Key R&D Program of China (No. 2022YFE0108800), the National Natural Science Foundation of China (Nos. 51832005, 51802274, 62075203, and U2005213), and Foreign

Coorperation Project of Fujian Provincial Science and Technology Plan (No. 2020I0002).

References

[1] Wang L, Xie RJ, Suehiro T, *et al*. Down-conversion nitride materials for solid state lighting: Recent advances and perspectives. *Chem Rev* 2018, **118**: 1951–2009.

[2] Zeuner M, Pagano S, Schnick W. Nitridosilicates and oxonitridosilicates: From ceramic materials to structural and functional diversity. *Angew Chem Int Ed* 2011, **50**: 7754–7775.

[3] Hirosaki N, Xie RJ, Kimoto K, *et al*. Characterization and properties of green-emitting β-SiAlON:Eu^{2+} powder phosphors for white light-emitting diodes. *Appl Phys Lett* 2005, **86**: 211905.

[4] Li YQ, Delsing ACA, de With G, *et al*. Luminescence properties of Eu^{2+}-activated alkaline-earth silicon-oxynitride $MSi_2O_{2-\delta}N_{2+2/3\delta}$ (M = Ca, Sr, Ba): A promising class of novel LED conversion phosphors. *Chem Mater* 2005, **17**: 3242–3248.

[5] Xie RJ, Hirosaki N, Mitomo M, *et al*. Photoluminescence of rare-earth-doped Ca-α-SiAlON phosphors: Composition and concentration dependence. *J Am Ceram Soc* 2005, **88**: 2883–2888.

[6] Duan CJ, Wang XJ, Otten WM, *et al*. Preparation, electronic structure, and photoluminescence properties of Eu^{2+}- and Ce^{3+}/Li^{+}-activated alkaline earth silicon nitride $MSiN_2$ (M = Sr, Ba). *Chem Mater* 2008, **20**: 1597–1605.

[7] Li JW, Watanabe T, Sakamoto N, *et al*. Synthesis of a multinary nitride, Eu-doped $CaAlSiN_3$, from alloy at low temperatures. *Chem Mater* 2008, **20**: 2095–2105.

[8] Li YQ, Hirosaki N, Xie RJ, *et al*. Yellow–orange-emitting $CaAlSiN_3$:Ce^{3+} phosphor: Structure, photoluminescence, and application in white LEDs. *Chem Mater* 2008, **20**: 6704–6714.

[9] Li HL, Xie RJ, Hirosaki N, *et al*. Synthesis and luminescence properties of orange–red-emitting $M_2Si_5N_8$:Eu^{2+} (M = Ca, Sr, Ba) light-emitting diode conversion phosphors by a simple nitridation of MSi_2. *Int J Appl Ceram Tec* 2009, **6**: 459–464.

[10] Liu LH, Xie RJ, Hirosaki N, *et al*. Temperature dependent luminescence of yellow-emitting α-SiAlON:Eu^{2+} oxynitride phosphors for white light-emitting diodes. *J Am Ceram Soc* 2009, **92**: 2668–2673.

[11] Braun C, Seibald M, Börger SL, *et al*. Material properties and structural characterization of $M_3Si_6O_{12}N_2$:Eu^{2+} (M = Ba, Sr)—A comprehensive study on a promising green phosphor for pc-LEDs. *Chem-Eur J* 2010, **16**: 9646–9657.

[12] Ryu JH, Won HS, Park YG, *et al*. Photoluminescence of Ce^{3+}-activated β-SiAlON blue phosphor for UV-LED. *Electrochem Solid St* 2010, **13**: H30–H32.

[13] Wang XM, Wang CH, Kuang XJ, *et al*. Promising oxonitridosilicate phosphor host $Sr_3Si_2O_4N_2$: Synthesis, structure, and luminescence properties activated by Eu^{2+} and Ce^{3+}/Li^{+} for pc-LEDs. *Inorg Chem* 2012, **51**: 3540–3547.

[14] Park WB, Shin N, Hong KP, *et al*. A new paradigm for materials discovery: Heuristics-assisted combinatorial chemistry involving parameterization of material novelty. *Adv Funct Mater* 2012, **22**: 2258–2266.

[15] Miao SH, Xia ZG, Molokeev MS, *et al*. Crystal structure refinement and luminescence properties of blue–green-emitting $CaSrAl_2SiO_7$:Ce^{3+},Li^{+},Eu^{2+} phosphors. *J Mater Chem C* 2015, **3**: 8322–8328.

[16] Wang ZB, Chu IH, Zhou F, *et al*. Electronic structure descriptor for the discovery of narrow-band red-emitting phosphors. *Chem Mater* 2016, **28**: 4024–4031.

[17] Zhuo Y, Mansouri Tehrani A, Oliynyk AO, *et al*. Identifying an efficient, thermally robust inorganic phosphor host via machine learning. *Nat Commun* 2018, **9**: 4377.

[18] Park WB, Singh SP, Yoon C, *et al*. Eu^{2+} luminescence from 5 different crystallographic sites in a novel red phosphor, $Ca_{15}Si_{20}O_{10}N_{30}$:$Eu^{2+}$. *J Mater Chem* 2012, **22**: 14068–14075.

[19] Park WB, Jeong YS, Singh SP, *et al*. A yellow-emitting oxynitride phosphor: $Ce_{4-x}Ca_xSi_{12}O_{3+x}N_{18-x}$:$Eu^{2+}$. *ECS J Solid State Sci Technol* 2013, **2**: R3100–R3106.

[20] Park WB, Singh SP, Yoon C, *et al*. Combinatorial chemistry of oxynitride phosphors and discovery of a novel phosphor for use in light emitting diodes, $Ca_{1.5}Ba_{0.5}Si_5N_6O_3$:$Eu^{2+}$. *J Mater Chem C* 2013, **1**: 1832–1839.

[21] Park WB, Singh SP, Sohn KS. Discovery of a phosphor for light emitting diode applications and its structural determination, $Ba(Si,Al)_5(O,N)_8$:Eu^{2+}. *J Am Chem Soc* 2014, **136**: 2363–2373.

[22] Liao HX, Zhao M, Molokeev MS, *et al*. Learning from a mineral structure toward an ultra-narrow-band blue-emitting silicate phosphor $RbNa_3(Li_3SiO_4)_4$:Eu^{2+}. *Angew Chem Int Ed* 2018, **130**: 11902–11905.

[23] Zhao M, Liao HX, Ning LX, *et al*. Next-generation narrow-band green-emitting $RbLi(Li_3SiO_4)_2$:Eu^{2+} phosphor for backlight display application. *Adv Mater* 2018, **30**: 1802489.

[24] Liao HX, Zhao M, Zhou YY, *et al*. Polyhedron transformation toward stable narrow-band green phosphors for wide-color-gamut liquid crystal display. *Adv Funct Mater* 2019, **29**: 1901988.

[25] Zhao M, Zhou YY, Molokeev MS, *et al*. Discovery of new narrow-band phosphors with the UCr_4C_4-related type structure by alkali cation effect. *Adv Opt Mater* 2019, **7**: 1801631.

[26] Pust P, Hintze F, Hecht C, *et al*. Group (III) nitrides $M[Mg_2Al_2N_4]$ (M = Ca, Sr, Ba, Eu) and $Ba[Mg_2Ga_2N_4]$—Structural relation and nontypical luminescence properties of Eu^{2+} doped samples. *Chem Mater* 2014, **26**: 6113–6119.

[27] Pust P, Weiler V, Hecht C, *et al*. Narrow-band red-emitting $Sr[LiAl3N_4]$:Eu^{2+} as a next-generation LED-phosphor material. *Nat Mater* 2014, **13**: 891–896.

[28] Pust P, Wochnik AS, Baumann E, *et al*. $Ca[LiAl3N_4]$:Eu^{2+}—A narrow-band red-emitting nitridolithoaluminate. *Chem Mater* 2014, **26**: 3544–3549.

[29] Wagatha P, Weiler V, Schmidt PJ, *et al*. Tailoring emission characteristics: Narrow-band red luminescence from SLA to CaBa[$Li_2Al_6N_8$]:Eu^{2+}. *Chem Mater* 2018, **30**: 7885–7891.

[30] Ha J, Kim YH, Novitskaya E, *et al*. Color tunable single-phase Eu^{2+} and Ce^{3+} co-activated Sr_2LiAlO_4 phosphors. *J Mater Chem C* 2019, **7**: 7734–7744.

[31] Li SX, Xia YH, Amachraa M, *et al*. Data-driven discovery of full-visible-spectrum phosphor. *Chem Mater* 2019, **31**: 6286–6294.

[32] Hirosaki N, Takeda T, Funahashi S, *et al*. Discovery of new nitridosilicate phosphors for solid state lighting by the single-particle-diagnosis approach. *Chem Mater* 2014, **26**: 4280–4288.

[33] Wang XJ, Wang L, Takeda T, *et al*. Blue-emitting $Sr_3Si_{8-x}Al_xO_{7+x}N_{8-x}$:$Eu^{2+}$ discovered by a single-particle-diagnosis approach: Crystal structure, luminescence, scale-up synthesis, and its abnormal thermal quenching behavior. *Chem Mater* 2015, **27**: 7689–7697.

[34] Ten Kate OM, Xie RJ, Wang CY, *et al*. Eu^{2+}-doped $Sr_2B_{2-2x}Si_{2+3x}Al_{2-x}N_{8+x}$: A boron-containing orange-emitting nitridosilicate with interesting composition-dependent photoluminescence properties. *Inorg Chem* 2016, **55**: 11331–11336.

[35] Wang CY, Takeda T, ten Kate OM, *et al*. New deep-blue-emitting Ce-doped $A_{4-m}B_nC_{19+2m}X_{29+m}$ (A = Sr, La; B = Li; C = Si, Al; X = O, N; $0 \leqslant m \leqslant 1$; $0 \leqslant n \leqslant 1$) phosphors for high-color-rendering warm white light-emitting diodes. *ACS Appl Mater Interfaces* 2019, **11**: 29047–29055.

[36] Zhang YX, Li SX, Takeda T, *et al*. Realizing red/orange emission of Eu^{2+}/Ce^{3+} in $La_{26-x}Sr_xSi_{41}O_{x+1}N_{80-x}$ (x = 12.72–12.90) phosphors for high color rendition white LEDs. *J Mater Chem C* 2020, **8**: 13458–13466.

[37] Yao FF, Wang L, Lv Y, *et al*. Composition-dependent thermal degradation of red-emitting $(Ca_{1-x}Sr_x)AlSiN_3$:Eu^{2+} phosphors for high color rendering white LEDs. *J Mater Chem C* 2018, **6**: 890–898.

[38] Kim Y, Kim J, Kang S. First-principles thermodynamic calculations and experimental investigation of Sr–Si–N–O system—Synthesis of $Sr_2Si_5N_8$:Eu phosphor. *J Mater Chem C* 2013, **1**: 69–78.

[39] Wu YP, Lu H, Wang SS, *et al*. Asymmetric boron-complexes containing keto-isoindolinyl and pyridyl groups: Solvatochromic fluorescence, efficient solid-state emission and DFT calculations. *J Mater Chem C* 2015, **3**: 12281–12289.

[40] Strobel P, de Boer T, Weiler V, *et al*. Luminescence of an oxonitridoberyllate: A study of narrow-band cyan-emitting Sr[Be_6ON_4]:Eu^{2+}. *Chem Mater* 2018, **30**: 3122–3130.

[41] Li SX, Amachraa M, Chen C, *et al*. Efficient near-infrared phosphors discovered by parametrizing the Eu(II) 5d-to-4f energy gap. *Matter* 2022, **5**: 1924–1936.

[42] Xie RJ, Hirosaki N, Sakuma K, *et al*. Eu^{2+}-doped Ca-α-SiAlON: A yellow phosphor for white light-emitting diodes. *Appl Phys Lett* 2004, **84**: 5404–5406.

[43] Qin X, Liu XW, Huang W, *et al*. Lanthanide-activated phosphors based on 4f–5d optical transitions: Theoretical and experimental aspects. *Chem Rev* 2017, **117**: 4488–4527.

[44] Ueda J, Dorenbos P, Bos AJJ, *et al*. Insight into the thermal quenching mechanism for $Y_3Al_5O_{12}$:Ce^{3+} through thermoluminescence excitation spectroscopy. *J Phys Chem C* 2015, **119**: 25003–25008.

[45] Li SX, Wang L, Tang DM, *et al*. Achieving high quantum efficiency narrow-band β-SiAlON:Eu^{2+} phosphors for high-brightness LCD backlights by reducing the Eu^{3+} luminescence killer. *Chem Mater* 2018, **30**: 494–505.

[46] Liu XJ, Li HL, Xie RJ, *et al*. Cerium-doped lutetium aluminum garnet optically transparent ceramics fabricated by a sol–gel combustion process. *J Mater Res* 2006, **21**: 1519–1525.